

## Peripheral ligands as electron storage reservoirs and their role in enhancement of photocatalytic hydrogen generation

Qing Pan, Leon Freitag, Tanja Kowacs, Jane C. Falgenhauer, Jeroen P. Korterik, Derck Schlettwein, Wesley R. Browne, Mary T. Pryce, Sven Rau, Leticia González, Johannes G. Vos and Annemarie Huijser

### Supporting Information

<b>S1 Experimental methods</b> .....	<b>2</b>
Synthesis, structural characterisation and hydrogen generation.....	2
Absorption and emission measurements.....	2
Density Functional Theory calculations.....	2
Time-resolved spectroscopy.....	3
<b>S2 Absorption/emission under normal and reduction conditions</b> .....	<b>4</b>
Normal conditions .....	4
Reduction conditions.....	6
<b>S3 Supplementary Density Functional Theory results</b> .....	<b>7</b>
<b>S4 Supplementary transient absorption data</b> .....	<b>10</b>
<b>S5 Role of the sacrificial agent</b> .....	<b>13</b>
<b>References</b> .....	<b>14</b>

## S1 Experimental methods

### Synthesis, structural characterisation and hydrogen generation

Details regarding the synthesis, structural characterisation and hydrogen generation experiments of **Ru**, **EtOOCRu**, **RuPt** and **EtOOCRuPt** are provided in reference 1.

### Absorption and emission measurements

Steady-state absorption spectra were recorded at room temperature using a SHIMADZU UV-1800 spectrophotometer with samples dissolved in acetonitrile (Sigma-Aldrich, purity >99.5%, spectroscopic grade) in 1 cm path length quartz cuvettes. Steady-state emission spectra were obtained at room temperature using a Horiba Jobin Yvon FluoroMax-4 spectrofluorometer with excitation at 450 nm. The solutions for differential absorption spectra under reduction condition consisted of the respective Ru compound dissolved in dimethyl sulfoxide (DMSO; Roth, purity  $\geq 99.5\%$ ,  $\leq 200$  ppm H<sub>2</sub>O) with 0.5 M of tetra-n-butylammoniumtetrafluoroborate (TBABF<sub>4</sub>; Merck-Schuchardt, purity  $\geq 98\%$ ) added as supporting electrolyte. The solution was purged with N<sub>2</sub> prior to and during the measurement. An ITO-covered glass substrate (Indium Tin Oxide; Delta Technologies, sheet resistance 8-12  $\Omega$ /sq) served as the working electrode. The ITO was covered with an uncoated glass (Roth) leaving a thin layer of electrolyte in front of it, which was lifted above the electrolyte level by capillary forces forming a transparent thin layer cell. A leak-free LF-2 reference electrode (Warner Instruments, 242 mV vs. NHE) and a platinum wire counter electrode (Aldrich, purity 99.99%) were used. A diode array spectrometer setup (LS-C H lamp, LOE-USB MMS 1 spectrometer from Tec5) was used to analyse transmission changes in the thin layer cell while the electrochemical measurement was performed using an IviumStat potentiostat (IVIUM Technologies). Various voltages were applied to the thin layer of the solution. The differential absorption spectra were measured assuming no changes in reflection.

### Density Functional Theory calculations

Geometry optimisations of the singlet ground and lowest triplet states of all complexes were performed using Density Functional Theory (DFT). For the ground state, the BP86<sup>2, 3</sup> functional was employed; to speed up the computations the RI-J and MARIJ<sup>4</sup> approximations were used. The calculations were performed with TURBOMOLE 6.6.<sup>5</sup> For the geometries of the lowest triplet states, B3LYP<sup>3, 6</sup> functional and the Gaussian 09<sup>7</sup> program package were used. Higher triplet states were optimised with the time-dependent DFT (TD-DFT) formalism. In all DFT calculations, the D3 dispersion correction by Grimme and co-workers<sup>8</sup> and the def2-SVP<sup>9</sup> basis set were used. For Ru, Pt and I, the Stuttgart-Dresden quasi-relativistic effective core potential (MWB)<sup>10</sup> with 28, 46 and 60 electrons, respectively, was employed. To incorporate solvent effects (acetonitrile) in the calculation of triplet energy gaps, at each optimised triplet geometry single-point (non-time-dependent) DFT calculations with the same functional and basis set as in the optimisations, but additionally employing the integral equation formalism (IEF)<sup>11, 12</sup> of the polarisable continuum model (PCM)<sup>13, 14</sup> were performed. In addition, in all geometries one acetonitrile molecule has been coordinated to the Pt centre as the solvent molecule. To analyse the ground state absorption, for each complex an electronic absorption spectrum was calculated for the 60 lowest excited

states with TD-DFT employing the B3LYP functional with the RIJCOSX approximation<sup>15, 16</sup> and the COSMO<sup>17, 18</sup> implicit solvation model for acetonitrile with the ORCA 3.0.2 program package.<sup>19</sup>

### **Time-resolved spectroscopy**

The femtosecond transient absorption (TA) setup was described earlier.<sup>20</sup> The instrumental response time was estimated from the coherent artifact signal from the solvent to be ~120 fs in the blue part of the visible and ~200 fs at 360 nm. The complexes were dissolved in anhydrous acetonitrile (Sigma-Aldrich, purity >99.9%) with ca. 0.4 mM concentration in 1 mm path length quartz cuvettes and excited at 480 nm (~50 fs pulse duration, FWHM bandwidth of 7 nm). The pulse energy of the pump was ca.  $4 \times 10^{14}$  photons/cm<sup>2</sup> and verified to be in the linear regime. A white light continuum generated by focusing a part of the fundamental 775 nm beam into a CaF<sub>2</sub> crystal was used as probe. The polarisation angle between the pump and probe beams was set at magic angle (54.7°). The possibility of pump-induced degradation was excluded by comparing the final measurement with the first measurement, which data are similar. The TA data were numerically corrected for chirp and analysed using the open-source program Glotaran.<sup>21</sup>

Time-resolved photoluminescence data were recorded at room temperature using a FluoroMax Spectrofluorometer extended for time-correlated single photon counting (TCSPC) measurements (HORIBA JOBIN YVON, FluoroMax-4 TCSPC). A NanoLED-460 laser (462 nm, 1.3 ns pulse duration) was used for excitation. The compounds **Ru**, **RuPt** and **EtOOCRuPt** were excited at a repetition rate of 100 kHz, **EtOOCRu** was measured at 50 kHz repetition rate.

## S2 Absorption/emission under normal and reduction conditions

### Normal conditions

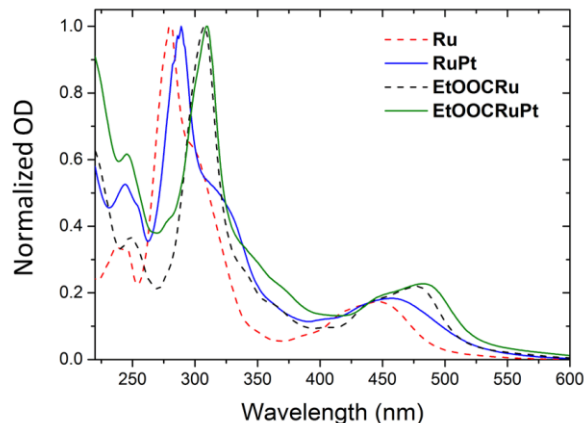


**Figure S2-1.** Normalized optical density (OD) spectra of **Ru**, **RuPt**, **EtOOCRu** and **EtOOCRuPt** in acetonitrile.

Figure S2-1 shows the steady-state optical density (OD) spectra of all complexes studied dissolved in acetonitrile. The broad bands from 400 nm to 600 nm, common for Ru(II)-polypyridyl complexes, are best described as metal-to-ligand charge transfer (MLCT) transitions.<sup>22-25</sup> Photoexcitation in this spectral window causes an electron to be excited from the d orbital of the Ru(II) atom towards the ligands. The absorption bands around 300 nm are more complex than simple ligand centred (LC)  $\pi-\pi^*$  descriptions<sup>24, 26</sup> of the (EtOOC-)bpy and tpy ligands.<sup>20, 27</sup> In fact, these transitions involve a mixture of LC, MLCT, and LLCT (ligand-to-ligand charge transfer) behaviours calculated using DFT. Upon functionalisation of the peripheral bpy ligands with EtOOC groups, both the mononuclear **EtOOCRu** and the dinuclear **EtOOCRuPt** undergo a redshift in absorption as compared to their non-functionalised counterparts **Ru** and **RuPt**.

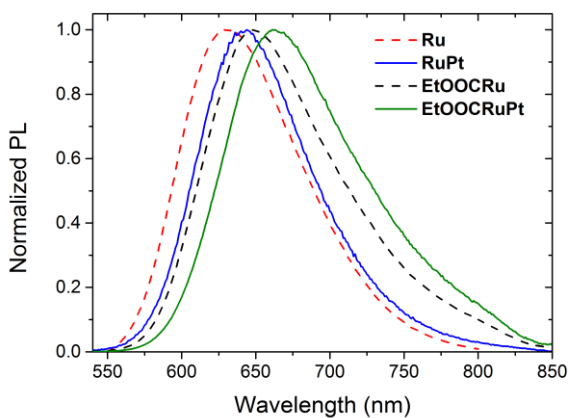


**Figure S2-2.** Steady-state photoluminescence (PL) spectra of **Ru**, **RuPt**, **EtOOCRu** and **EtOOCRuPt** in acetonitrile, recorded at  $\lambda_{exc} = 450$  nm.

The normalised steady-state photoluminescence (PL) spectra (Figure S2-2) show that the bands of both **RuPt** and **EtOOCRuPt** are redshifted compared to their mononuclear Ru precursors, indicating that Pt cyclometallation reduces the energy gap between the ground state and the lowest excited state. The MLCT absorption and emission maxima are summarised in Table S2-1.

**Table S2-1.** The maxima of the MLCT absorption and PL bands.

	<b>Ru</b>	<b>RuPt</b>	<b>EtOOCRu</b>	<b>EtOOCRuPt</b>
$\lambda_{\text{abs}}$	446 nm	457 nm	477 nm	482 nm
$\lambda_{\text{em}}$	630 nm	644 nm	648 nm	663 nm

## Reduction conditions

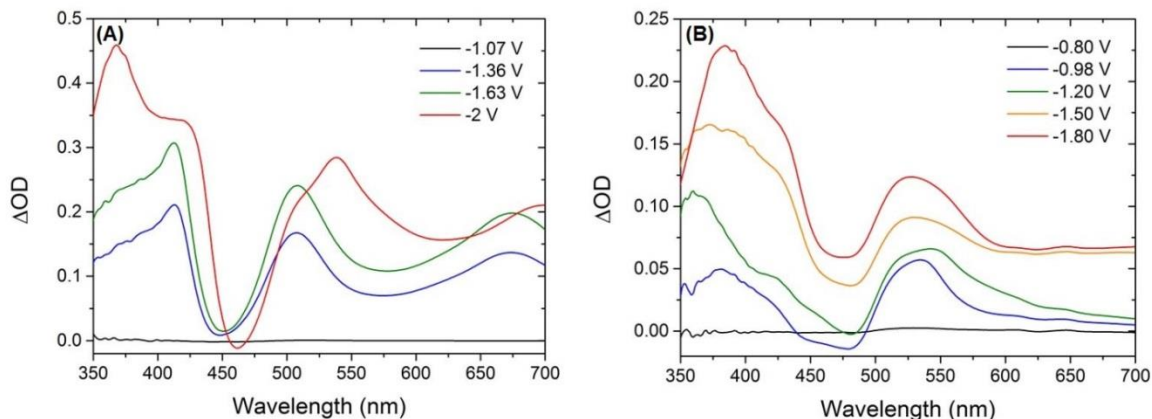


**Figure S2-3.** Differential optical density ( $\Delta OD$ ) spectra of **Ru** (A) and **EtOOCRu** (B) at various reduction potentials (vs. Ag/AgCl). The spectrum at each potential was recorded after applying the voltage for 10 minutes and corrected for the steady-state absorption at zero applied bias.

In addition to the DFT calculations discussed in the main text, the impact of the EtOOC groups on the energy levels of the complexes has also been studied using UV/vis differential absorption under electrochemical reduction conditions. Although under these conditions the reduced species is detected rather than the  $^3MLCT$  excited states, in both cases the same  $\pi^*$  orbital is involved.

The differential absorption spectra of **Ru** and **EtOOCRu** at various reduction potentials are shown in Figure S2-3. For **Ru** two absorption bands (one at ca. 360 nm and another at ca. 420 nm) are well distinguishable, in agreement with the TA spectra.<sup>20</sup> The band at ca. 360 nm is likely due to the reduced bpy ligand<sup>28</sup> and close to the excited state absorption band around 370 nm observed in TA.<sup>20, 29</sup> Analogously, the band around 420 nm is likely due to the reduced tpy ligand. Initially, at -1.07 V neither bpy nor tpy is reduced (Figure A) and no absorption difference compared to the spectrum at 0 V exists. On moving towards more negative potentials (-1.36 V and -1.63 V) predominantly the tpy $^-$  band starts appearing, while at -2.00 V the bpy $^-$  band has become more intense than the tpy $^-$  band. These results indicate that for **Ru** reduction of the bpy ligand requires a more negative potential than for the tpy ligand, indicating that the bpy-based  $\pi^*$  orbital is higher in energy than the tpy-based one.

The situation for **EtOOCRu** is different. Differential absorption features appear at a less negative applied potential as compared to **Ru**, indicating that the EtOOC groups lower the energy levels. This conclusion is in agreement with the redshift in steady-state absorption (Figure S2-1). Throughout all applied negative applied potentials (down to -1.80 V), both EtOOC-bpy $^-$  and tpy $^-$  contribute to the differential absorption. This result indicates that the EtOOC-bpy and tpy ligands require rather similar negative potentials to become reduced.

### S3 Supplementary Density Functional Theory results

Table S3-1 shows the calculated energy of the bright  $^1\text{MLCT}(\text{d}(\text{Ru}) \rightarrow (\text{EtOOC-})\text{bpy } \pi^*)$  transition for all complexes. This transition undergoes a redshift of 0.18 eV for the mononuclear and 0.25 eV for the dinuclear complexes. The Lowest Unoccupied Molecular Orbital (LUMO) calculated at the ground state geometry (see Figure S3-1) has tpy  $\pi^*$  character for **Ru** and **RuPt**, but is of EtOOC-bpy (EtOOC-bpy)  $\pi^*$  character for **EtOOCRu** and **EtOOCRuPt**. A similar trend is followed by the lowest singlet excited state ( $S_1$ , always dark), which has  $^1\text{MLCT}(\text{d}(\text{Ru}) \rightarrow \text{tpy } \pi^*)$  character in the non-functionalised complexes, however upon ester functionalisation the  $\pi^*$  orbital gains EtOOC-bpy character. In conclusion, the EtOOC groups change the energetics of the individual singlet excited states, causing the  $^1\text{MLCT}(\text{d}(\text{Ru}) \rightarrow \text{EtOOC-bpy } \pi^*)$  state to become lower in energy than the  $^1\text{MLCT}(\text{d}(\text{Ru}) \rightarrow \text{tpy } \pi^*)$  state.

**Table S3-1.** Calculated energies of the bright MLCT ( $\text{d}(\text{Ru}) \rightarrow (\text{EtOOC-})\text{bpy } \pi^*$ ) transitions.

<b>Ru</b>	<b>EtOOCRu</b>	<b>RuPt</b>	<b>EtOOCRuPt</b>
2.87 eV (432 nm)	2.69 eV (461 nm)	2.83 eV (438 nm)	2.58 eV (481 nm)

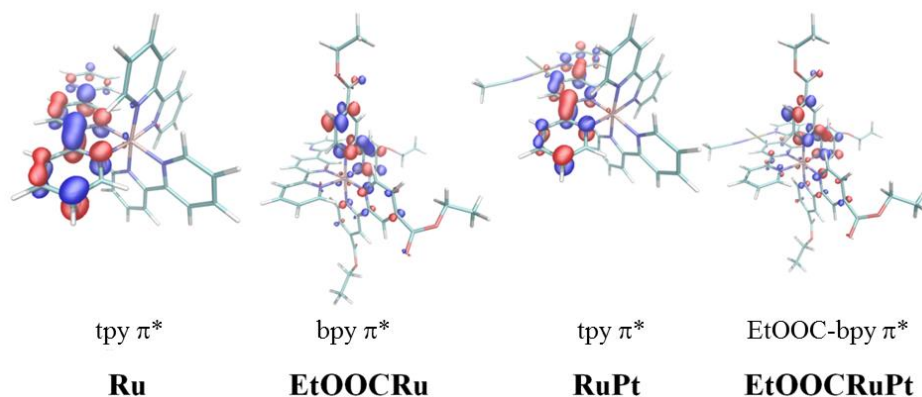


**Figure S3-1.** LUMO of **Ru**, **EtOOCRu**, **RuPt** and **EtOOCRuPt** calculated at the electronic ground state geometry.

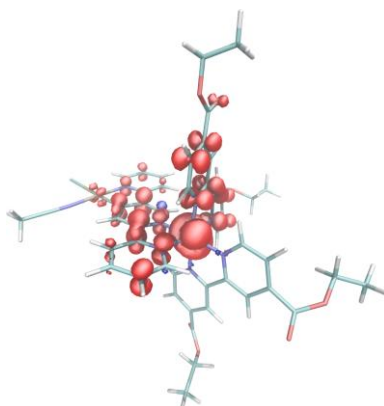


**Figure S3-2.** Spin density of the tpy-based triplet state of the **EtOOCRuPt** complex.

As discussed in the main text, equilibration processes are observed between the  $^3\text{MLCT}$  states localised on the individual ligands. Although activation barriers have not been calculated, conclusions about the barrier can be drawn by comparing the (EtOOC-)bpy and tpy triplet geometries, which are fairly similar and do not show any large conformational change or other significant geometric rearrangements. The root-mean-square deviation (RMSD) between the (EtOOC-)bpy and tpy structures in each complex is less than 0.27 Å. This result suggests that the activation barrier between the (EtOOC-)bpy and tpy triplet states is low and population redistribution between the states may easily occur. This rebalancing is likely accompanied by vibrational cooling. However, the cyclometalated complexes **RuPt** and **EtOOCRuPt** exhibit larger RMSD(bpy-tpy) values than their corresponding mononuclear Ru precursors.

**Table S3-2.** Lowest triplet excited states, energy gaps and RMSD between geometries for the tpy-and (EtOOC)bpy-localized triplet excited states.

	<b>Ru</b>	<b>EtOOCRu</b>	<b>RuPt</b>	<b>EtOOCRuPt</b>
<b>lowest triplet</b>	tpy	EtOOC-bpy	tpy	EtOOC-bpy
<b><math>\Delta E(\text{bpy-tpy})/\text{eV}</math></b>	0.13	-0.30	0.18	-0.10
<b><math>\text{RMSD}(\text{bpy-tpy})/\text{Å}</math></b>	0.206	0.203	0.259	0.269

Although calculation of the absolute energetics at the excited triplet states is challenging, the present DFT results suggest that stabilisation of the bpy triplet state upon EtOOC functionalisation appears to be more pronounced in the precursors: in **EtOOCRu** the bpy state is stabilised by 0.43 eV compared to **Ru**, resulting in a gap of 0.30 eV between the two ligand-based triplet states. This trend remains nevertheless the same for the dinuclear complexes, although with a smaller gap. In all cases the gap exceeds kT at room temperature, indicating that an excited state equilibrium is shifted to the tpy state in **Ru** and **RuPt**, and to the EtOOC-bpy state in **EtOOCRu** and **EtOOCRuPt**.

### Notes on isomerism of RuPt and EtOOCRuPt

As discussed in the main text, the **RuPt** and **EtOOCRuPt** complexes may form coordination isomers with swapped S and X ligands (see Fig. 1), denoted as **cis-RuPt** and **cis-EtOOCRuPt**. The calculated ground state energy of **cis-RuPt** is 1.06 kcal/mol lower than that of **RuPt**. The calculated absorption spectra of **RuPt** and **cis-RuPt** are very similar, which also applies to **EtOOCRuPt** and **cis-EtOOCRuPt**. Based on these phenomena, we propose that both **RuPt** and **cis-RuPt** may be present in solution. Unlike in **RuPt**, the lowest triplet state of **cis-RuPt** is a d(Ru)→bpy  $\pi^*$  MLCT state, similar to **EtOOCRu**. Yet, its energy gap to the ground state is similar and is also lowered by a similar amount of energy upon substitution with the EtOOC groups, as shown in Table S3-3.

**Table S3-3.** Singlet-bpy triplet gaps for **RuPt**, **EtOOCRuPt** and their isomers.

	<b>RuPt</b>	<b>EtOOCRuPt</b>	<b>cis-RuPt</b>	<b>cis-EtOOCRuPt</b>
<b><math>\Delta E(\text{bpy-tpy})/\text{eV}</math></b>	2.09	1.97	2.05	1.94

## S4 Supplementary transient absorption data

The kinetic traces ( $\Delta OD$  vs. time at key wavelengths) of **EtOOCRu** are shown in Figure S4-1. The photophysical model for fitting the TA data is presented in Figure S4-2, and the obtained species associated spectra are provided in Figure S4-3. The intense excited state absorption (ESA) band at ca. 420 nm is assigned to the absorption of the reduced tpy ligand, and the two ESA bands in the UV region (one at ca. 385 nm and another one at ca. 350 nm) are likely due to the reduced EtOOC-bpy ligands (see main text). The broad ESA signal above 520 nm is due to ligand-to-metal charge transfer (LMCT) transitions. Note that after the initial ultrafast equilibration, the TA spectra do not change significantly until at least 6 ns (Figure S4-4). The spike signal within 250 fs observed in Figure S4-1 (B) is due to a coherent artifact and is therefore not included in the fit.

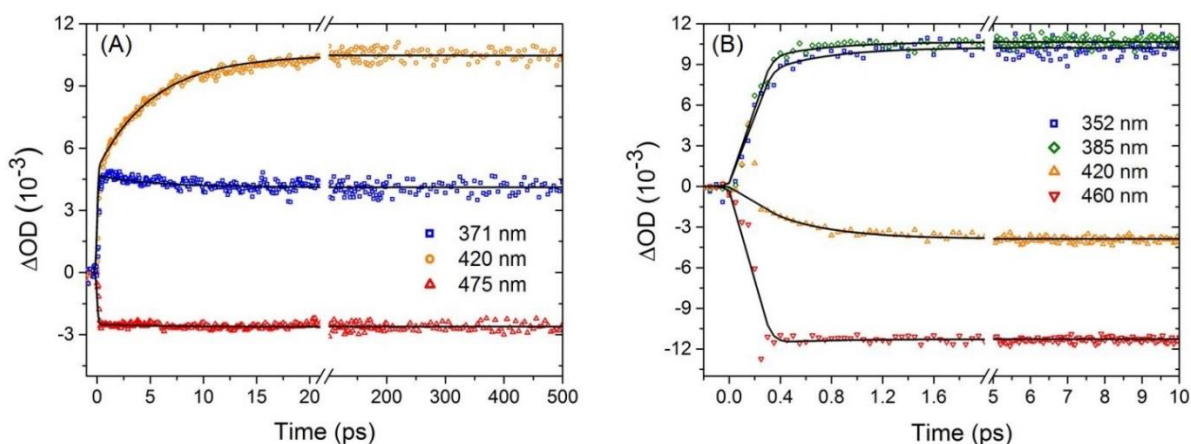


**Figure S4-1.** Kinetic traces of  $\text{Ru}^{20}$  (A) and **EtOOCRu** (B), with fits represented as solid curves.

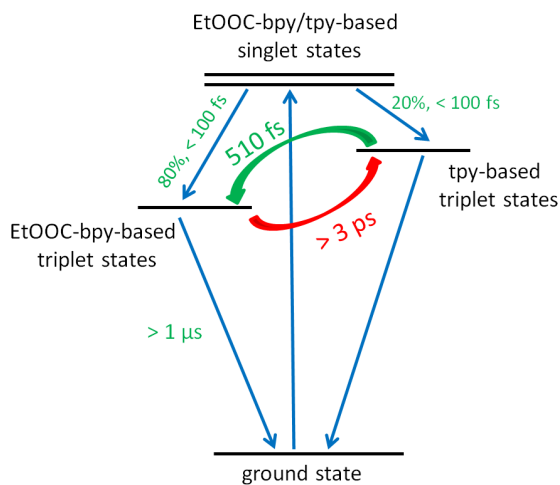


**Figure S4-2.** Simplified photophysical model of light-induced processes in **EtOOCRu**. The values are determined from target analysis of the TA data and the photoluminescence lifetimes.

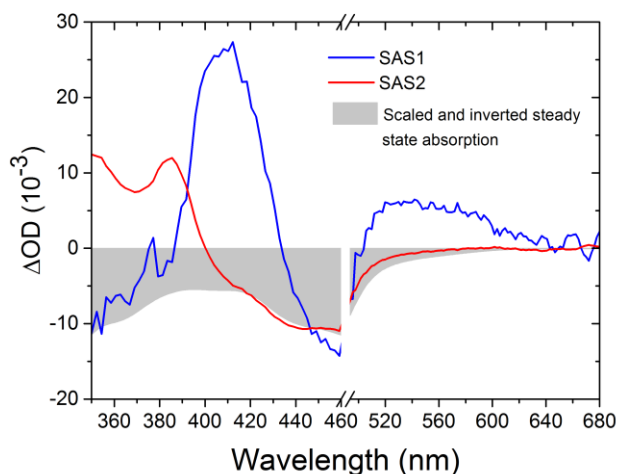


**Figure S4-3.** Species associated spectra of **EtOOCRu**. The grey area represents the scaled and inverted steady-state absorption spectrum. SAS1 consists of GSB and ESA ( $\text{tpy}^-$ ,  $\text{LMCT}_{\text{tpy}}$ ), while both GSB and ESA ( $\text{EtOOC-bpy}^-$ ,  $\text{LMCT}_{\text{EtOOC-bpy}}$ ) contribute to SAS2.

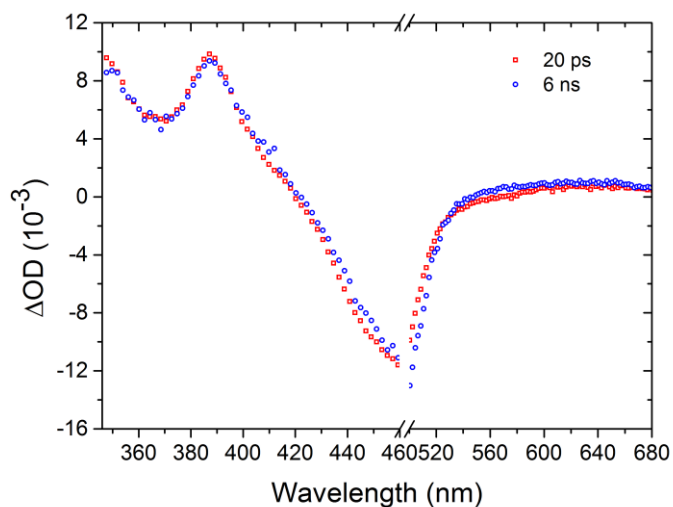


**Figure S4-4.** TA spectra of **EtOOCRu** at time delays of 20 ps and 6 ns.

The species associated spectra derived from target analysis of the TA data of **EtOOCRuPt** are shown in Figure S4-5. The inverted steady-state absorption is included as a grey area and overlaps with the ground state bleach (GSB) signal between 420 nm and 520 nm. The interpretation is analogous to **EtOOCRu**.

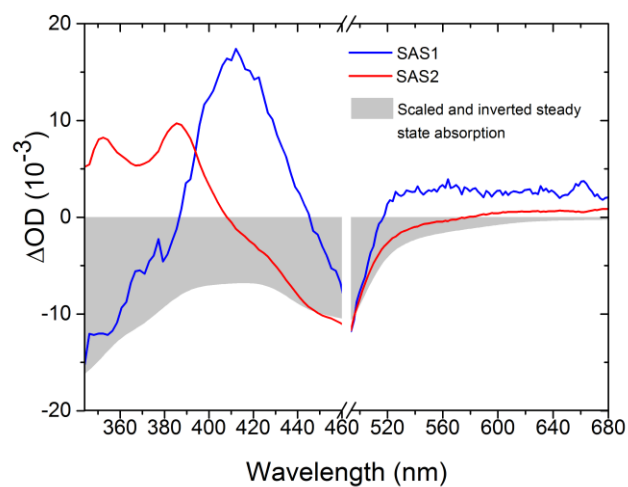
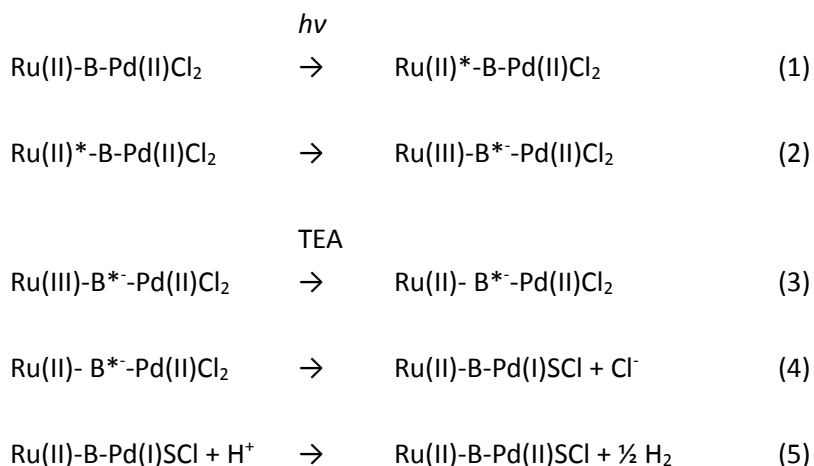


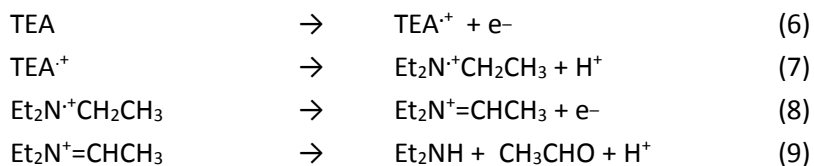
**Figure S4-5.** Species associated spectra of **EtOOCRuPt**. The grey area represents the scaled and inverted steady-state absorption spectrum. SAS1 consists of GSB and ESA ( $\text{tpy}^{\cdot-}$ ,  $\text{LMCT}_{\text{tpy}}$ ), while both GSB and ESA ( $\text{EtOOC-bpy}^{\cdot-}$ ,  $\text{LMCT}_{\text{EtOOC-bpy}}$ ) contribute to SAS2.

## S5 Role of the sacrificial agent

To further investigate the photocatalytic processes, detailed assessment of the photophysical properties are needed under catalytic conditions, however examples of such studies have so far rarely been reported. There are number of reasons for this, firstly the compounds studied are unlikely to be the real photocatalysts, but more likely “pre-photocatalysts” as is generally observed in catalytic studies. Secondly, and most importantly, the presence of the sacrificial agent triethylamine (TEA). After excitation of the photosensitiser, interaction with TEA leads to electron donation from the sacrificial agent to the formally Ru(III)-centre to regenerate the photosensitiser (see Scheme S5-1). The TEA decomposes after electron donation to the photosensitiser (Scheme S5-2). As a result, under photocatalytic conditions large amounts of radicals are formed, which may create side reactions by reacting with solvents, and a photophysical assessment is no longer possible.



**Scheme S5-1.** Proposed pathway for photocatalytic hydrogen generation by **RuPd**. B = bridging ligand, S = solvent. Analogous pathways may apply to **RuPt** and **EtOOCRuPt**. Note that photoexcitation and intersystem crossing not only lead to population of B (2), but also of the peripheral ligands.



**Scheme S5-2.** Decomposition pathway of TEA after electron donation to the photosensitiser.

Based on these issues, we report the photophysical behaviour of **RuPt** and **EtCOOCRuPt** on the ps timescale in anhydrous acetonitrile without TEA.

## References

1. T. Kowacs, Q. Pan, A. Huijser, S. Rau, P. Lang, W. R. Browne, M. T. Pryce and J. G. Vos, *Inorg. Chem.*, 2016, **55**, 2685-2690.
2. J. P. Perdew, *Phys. Rev. B*, 1986, **33**, 8822-8824.
3. A. D. Becke, *J. Chem. Phys.*, 1993, **98**, 5648-5652.
4. M. Sierka, A. Hogekamp and R. Ahlrichs, *J. Chem. Phys.*, 2003, **118**, 9136-9148.
5. TURBOMOLE V6.6, a development of University of Karlsruhe and Forschungszentrum Karlsruhe GmbH, 1989–2007, TURBOMOLE GmbH, since 2007; available at <http://www.turbomole.com>.
6. C. T. Lee, W. T. Yang and R. G. Parr, *Phys. Rev. B*, 1988, **37**, 785-789.
7. Gaussian 09, R. D. M. J. F., G. W. Trucks, H. B. Schlegel, G. E. Scuseria, M. A. Robb, J. R. Cheeseman, G. Scalmani, V. Barone, B. Mennucci, G. A. Petersson, H. Nakatsuji, M. Caricato, X. Li, H. P. Hratchian, A. F. Izmaylov, J. Bloino, G. Zheng, J. L. Sonnenberg, M. Hada, M. Ehara, K. Toyota, R. Fukuda, J. Hasegawa, M. Ishida, T. Nakajima, Y. Honda, O. Kitao, H. Nakai, T. Vreven, J. A. Montgomery, Jr., J. E. Peralta, F. Ogliaro, M. Bearpark, J. J. Heyd, E. Brothers, K. N. Kudin, V. N. Staroverov, R. Kobayashi, J. Normand, K. Raghavachari, A. Rendell, J. C. Burant, S. S. Iyengar, J. Tomasi, M. Cossi, N. Rega, J. M. Millam, M. Klene, J. E. Knox, J. B. Cross, V. Bakken, C. Adamo, J. Jaramillo, R. Gomperts, R. E. Stratmann, O. Yazyev, A. J. Austin, R. Cammi, C. Pomelli, J. W. Ochterski, R. L. Martin, K. Morokuma, V. G. Zakrzewski, G. A. Voth, P. Salvador, J. J. Dannenberg, S. Dapprich, A. D. Daniels, Ö. Farkas, J. B. Foresman, J. V. Ortiz, J. Cioslowski, and D. J. Fox, Gaussian, Inc., Wallingford CT, 2009.
8. S. Grimme, J. Antony, S. Ehrlich and H. Krieg, *J. Chem. Phys.*, 2010, **132**.
9. F. Weigend and R. Ahlrichs, *Phys. Chem. Chem. Phys.*, 2005, **7**, 3297-3305.
10. D. Andrae, U. Haussermann, M. Dolg, H. Stoll and H. Preuss, *Theor. Chim. Act.*, 1990, **77**, 123-141.
11. E. Cancès and B. Mennucci, *J. Math. Chem.*, 1998, **23**, 309-326.
12. B. Mennucci, E. Cancès and J. Tomasi, *J. Phys. Chem. B*, 1997, **101**, 10506-10517.
13. S. Miertus, E. Scrocco and J. Tomasi, *Chem. Phys.*, 1981, **55**, 117-129.
14. G. Scalmani and M. J. Frisch, *J. Chem. Phys.*, 2010, **132**.
15. F. Neese, F. Wennmohs, A. Hansen and U. Becker, *Chem. Phys.*, 2009, **356**, 98-109.
16. R. Izsak and F. Neese, *J. Chem. Phys.*, 2011, **135**.
17. A. Klamt and G. Schuurmann, *J. Chem. Soc. Trans. 2*, 1993, 799-805.
18. A. Klamt, *Interdisc. Rev. Comp. Mol. Sci.*, 2011, **1**, 699-709.
19. F. Neese, *Interdisc. Rev. Comp. Mol. Sci.*, 2012, **2**, 73-78.
20. Q. Pan, F. Mecozzi, J. P. Korterik, D. Sharma, J. L. Herek, J. G. Vos, W. R. Browne and A. Huijser, *J. Phys. Chem. C*, 2014, **118**, 20799-20806.
21. J. J. Snellenburg, S. P. Liptonok, R. Seger, K. M. Mullen and I. H. M. van Stokkum, *J. Stat. Softw.*, 2012, **49**, 1-22.
22. A. Juris, V. Balzani, F. Barigelletti, S. Campagna, P. Belser and A. Vonzelewsky, *Coord. Chem. Rev.*, 1988, **84**, 85-277.
23. A. Cannizzo, F. van Mourik, W. Gawelda, G. Zgrablic, C. Bressler and M. Chergui, *Angew. Chem. Int. Ed.*, 2006, **45**, 3174-3176.

24. K. Kalyanasundaram, *Coord. Chem. Rev.*, 1982, **46**, 159-244.
25. C. Daul, E. J. Baerends and P. Vernooijs, *Inorg. Chem.*, 1994, **33**, 3538-3543.
26. G. A. Heath, L. J. Yellowlees and P. S. Braterman, *J. Chem. Soc. Chem. Comm.*, 1981, 287-289.
27. G. S. Bindra, M. Schulz, A. Paul, R. Groarke, S. Soman, J. L. Inglis, W. R. Browne, M. G. Pfeffer, S. Rau, B. J. MacLean, M. T. Pryce and J. G. Vos, *Dalton Trans.*, 2012, **41**, 13050-13059.
28. M. Krejčík and A. A. Vlček, *J. Electroanal. Chem.*, 1991, **313**, 243-257.
29. S. Wallin, J. Davidsson, J. Modin and L. Hammarström, *J. Phys. Chem. A*, 2005, **109**, 4697-4704.